JGR Space Physics

RESEARCH ARTICLE
10.1029/2021JA029532

Observational Evidence of the Excitation of Magnetosonic Waves by an He^{++} Ion Ring Distribution

S. G. Claudepierre[1,2], X. Liu[3], L. Chen[3], and K. Takahashi[4]

[1]Space Sciences Department, The Aerospace Corporation, El Segundo, CA, USA, [2]Department of Atmospheric and Oceanic Sciences, UCLA, Los Angeles, CA, USA, [3]Department of Physics, University of Texas at Dallas, Richardson, TX, USA, [4]The Johns Hopkins University Applied Physics Laboratory, Laurel, MD, USA

Key Points:

- Equatorial magnetosonic waves are observed at harmonics of the He^{++} gyrofrequency near $L = 4$ on the dayside
- Particle observations suggest the presence of a helium ion ring distribution at energies ~30–300 keV
- Linear growth rate calculations indicate that the MS waves are generated from the unstable ring distribution

Supporting Information:

Supporting Information may be found in the online version of this article.

Correspondence to:

S. G. Claudepierre,
sethclaudepierre@atmos.ucla.edu

Citation:

Claudepierre, S. G., Liu, X., Chen, L., & Takahashi, K. (2021). Observational evidence of the excitation of magnetosonic waves by an He^{++} ion ring distribution. *Journal of Geophysical Research: Space Physics*, *126*, e2021JA029532. https://doi.org/10.1029/2021JA029532

Received 4 MAY 2021
Accepted 12 JUL 2021

Abstract We report plasma wave observations of equatorial magnetosonic waves at integer harmonics of the local gyrofrequency of doubly ionized helium (He^{++}). The waves were observed by Van Allen Probe A on 08 Feb 2014 when the spacecraft was in the afternoon magnetic local time sector near $L \approx 4$ inside of the plasmasphere. Analysis of the complementary in-situ energetic ion measurements (1–300 keV) reveals the presence of a helium ion ring distribution centered near 30 keV. Theoretical linear growth rate calculations suggest that the local plasma and field conditions can support the excitation of the magnetosonic waves from the unstable ring distribution. This represents the first report of the generation of magnetosonic equatorial noise via a ring distribution in energetic He^{++} ions in the near-Earth space plasma environment.

Plain Language Summary In nature, an object displaced from its stable equilibrium typically responds by oscillating at its natural frequency (e.g., a plucked guitar string). The ionized gas (plasma) in outer space where Earth-orbiting satellites fly is no different. In music, we have octaves or the overtone series of pure tones, where each frequency is an integer multiple of a fundamental. In this study, we report on such "musical notes" in space, but instead of sound waves propagating through air (music), these musical notes are propagating in the plasma in space. And while music is heard because of the sound waves compressing air, these space plasma waves are the result of subatomic particles oscillating about (and cannot be heard). The oscillating particles are helium atoms that have two of their electrons stripped away by the violent processes that occur near the Sun's surface. These particles have made their way through interplanetary space all the way to Earth where they are detected by sophisticated sensors on NASA's Van Allen Probe satellites.

1. Introduction

Magnetosonic (MS) waves, also known as equatorial noise (Russell et al., 1969, 1970), are electromagnetic emissions observed in the Earth's inner magnetosphere. The waves are found both inside and outside of the plasmasphere and are typically confined within a few degrees of the magnetic equator (e.g., Gurnett, 1976; Hrbáčková et al., 2015; Němec et al., 2005; Olsen et al., 1987; Santolík et al., 2004; Yuan et al., 2018). The waves occur above the proton gyrofrequency and below the lower hybrid resonance frequency, which in the inner magnetosphere corresponds to emissions in the ~1–100 Hz range. The wave magnetic field is nearly linearly polarized (along the background magnetic field, B_0) and the wave electric field is nearly perpendicular to B_0. We note that these MS waves are not to be confused with the "magnetosonic" mode in magnetohydrodynamic theory that propagates well below the ion cyclotron frequency (Santolík et al., 2016). It has been noted by Gary et al. (2010) that MS waves are perhaps more properly referred to as ion Bernstein waves, but here we will simply follow the nomenclature common in the literature.

In early observational work, it was established that MS waves propagate nearly perpendicular to the background magnetic field and consist of many discrete spectral lines with nearly equal spacing. Several of these studies (e.g., Gurnett, 1976; Perraut et al., 1982) demonstrated that MS waves occur as a series of narrow tones, spaced at multiples of the proton gyrofrequency, all the way up to the lower hybrid resonance frequency. The waves can also be observed as unstructured hiss-like emissions (Balikhin et al., 2015; Němec et al., 2015; Posch et al., 2015), though this may be a consequence of insufficient frequency resolution in the spectral measurements. Many years of satellite observations have revealed the global characteristics and

spectral features of MS waves in great detail, for example, from CRRES (Meredith et al., 2008), THEMIS (Ma et al., 2013), Cluster (Němec et al., 2013; Santolík et al., 2004), Polar (Tsurutani et al., 2014), and Van Allen Probes (Ma et al., 2016; Posch et al., 2015; Ouyang et al., 2021). In the MS mode, the dominant component of the wave magnetic field along B_0 has average amplitudes of ∼50 pT (Ma et al., 2013). Much more intense MS waves have also been reported with amplitudes up to ∼1 nT from Polar (Tsurutani et al., 2014) and from Van Allen Probes (Maldonado et al., 2016). High-resolution observations have revealed new, complex features, such as rising-tone spectra and quasi-periodicity in time (Boardsen et al., 2014; Fu et al., 2014; Němec et al., 2015).

From a theoretical perspective, it has been demonstrated that equatorial MS waves are excited at very oblique wave normal angles via an instability associated with an energetic proton ring-like or shell distribution. The free energy for the waves comes from a positive gradient ($\partial f / \partial v_\perp > 0$) in the velocity space distribution function, f, of energetic protons with ring velocity comparable to the Alfvén speed, typically near ∼1–30 keV (e.g., Chen, 2015; Curtis & Wu, 1979; Gary et al., 2010; Horne et al., 2000; Liu et al., 2011). This theoretical picture has been confirmed observationally in many studies (e.g., Balikhin et al., 2015; Boardsen et al., 1992; Chen et al., 2011; Meredith et al., 2008; Thomsen et al., 2011; Xiao et al., 2013). Observationally, proton rings and MS wave occurrence are generally associated with enhanced injection/AE activity, with higher occurrence rates on the dayside (Q. Zhou et al., 2021). Global simulation of ring current dynamics in the inner magnetosphere has demonstrated that proton rings form primarily due to energy-dependent drift and loss, and that the instability can occur over a broad spatial region inside $L \approx 6.6$ (Chen et al., 2010; Jordanova et al., 2012). Once generated, MS waves propagate perpendicularly away from the source region in both the azimuthal and radial directions (Chen & Thorne, 2012; Ma et al., 2014; Němec et al., 2013). The waves can propagate azimuthally near the plasmapause on a global scale (e.g., Kasahara et al., 1994), and also propagate radially inward and outward across the plasmapause boundary (Xiao et al., 2012), or be reflected by density irregularities at the plasmapause (X. Liu et al., 2018). Similarly, O^+ cyclotron harmonic waves have been reported (Usanova et al., 2016) and their excitation is attributed to a positive gradient ($\partial f / \partial v_\perp > 0$) in energetic O^+ ion distributions (Min et al., 2017; K. Liu et al., 2020). We note the very recent work of Min et al. (2020) who used a 2D particle-in-cell simulation to examine several key aspects of MS wave excitation and propagation.

MS waves are also known to contribute directly to ring current and radiation belt dynamics through resonant wave-particle interactions. A variety of interactions have been demonstrated with MS waves, such as electron acceleration to MeV energies (Horne & Thorne, 1998; Horne et al., 2000, 2007; Mourenas et al., 2013), proton precipitation that contributes to proton aurora in the upper atmosphere (Xiao et al., 2014), and the formation of "butterfly" angular distributions in 100s of keV electrons (Li et al., 2016; Maldonado et al., 2016; Yang et al., 2017; R. Zhou et al., 2020). These interactions represent important cross-species and cross-region couplings in the inner magnetosphere.

Nearly all of the observational reports and theoretical treatments of MS waves have focused on protons and O^+ as the ion species of interest. Here, we report an event where MS waves were generated at integer multiples of the local He^{++} gyrofrequency. We provide evidence that suggests that the free energy for the waves comes from an unstable He^{++} ion ring distribution. We believe that this is the first such report in the published literature, linking harmonic MS wave generation to energetic (10–100s keV) alpha particles in the inner magnetosphere. The remainder of the paper is structured as follows. In Section 2 we describe the instrumentation that is used to study the MS waves in-situ in the Earth's inner magnetosphere. The results are presented in Section 3, followed by a more in-depth discussion in Section 4, and concluding remarks are provided in Section 5.

2. Data and Methods

The primary data sources used in this study come from the instrumentation onboard the NASA Van Allen Probe spacecraft. The twin Van Allen Probes, launched in August of 2012, provided high resolution measurements of the fields, waves and plasma in the Earth's inner magnetosphere. The Probes' orbited through the ring current/radiation belt region ∼5–6 times per day with an apogee near 6 R_E and perigee at 600 km

altitude for most of the mission (Mauk et al., 2013). Science activities ended in July 2019 (Probe B) and October 2019 (Probe A) when the onboard propellant used for attitude control was exhausted.

For our analysis, magnetic field measurements are obtained from the tri-axial fluxgate magnetometer (MAG) sensor that was part of the Electric and Magnetic Field Instrument Suite and Integrated Science (EMFISIS) suite (Kletzing et al., 2013). In the present study, the high-resolution measurements are used, which provide the three-axis DC magnetic field vector at a time resolution of 64 samples-per-second (1 vector every 0.015625 s). The EMFISIS suite also provided a measure of the in-situ electron density, obtained from the High-Frequency Receiver (HFR) via inversion of the observed upper hybrid resonance frequency (Kurth et al., 2015). We use these measurements of the electron density rather than those obtained from the spacecraft potential, since the latter relies on an empirical relationship based on the former to produce accurate plasma densities (c.f., Hartley et al., 2018).

To resolve and analyze MS waves, we perform a series of post-processing steps on the raw MAG data to produce dynamic spectrograms from the measured fields. First, we transform the fields from the solar magnetic (SM) coordinate system into a field-aligned coordinate (FAC) system, where the z-axis is along the background magnetic field, the x-axis is in the radial direction (pointing outward from the center of the Earth to the spacecraft position) perpendicular to the magnetic field, and the y-axis completes the orthogonal set (pointing eastward/azimuthally). The background magnetic field direction in SM coordinates is obtained as the 101-point running-averaged value of the 1/64 s cadence magnetic field data. Following this, the high-resolution magnetic field data is detrended by subtracting the background magnetic field. Finally, we compute dynamic spectrograms on the FAC field components using a windowed fast Fourier transform, with a window size of 1024-point time series (i.e., time length = 16 s) and time-shifting of 60 points. These choices for the Fourier analysis parameters are in accordance with previous MS wave studies and sufficient to resolve MS waves in the DC MAG data (e.g., Maldonado et al., 2016).

We also make use of the DC electric field measurements from the Electric Field and Waves (EFW) instrument that flew on Van Allen Probes (Wygant et al., 2013). This double probe sensor consisted of pairs of spherical probes that measured the electric potential difference at either end of orthogonal booms. In the present study, we only use electric field data from the spin-plane booms, denoted as E_u and E_v, which lay approximately in the $y - z$ GSE plane. The highest-time resolution EFW DC electric field data were reported at 32 samples-per-second, which we process into dynamic spectrograms in a manner analogous to that described above for the MAG data, albeit without the rotation into FAC coordinates.

Our analysis also makes use of Van Allen Probe particle measurements. We obtain ion measurements at plasma energies (~1–50 keV) from the Helium, Oxygen, Proton, and Electron (HOPE) Mass Spectrometer (Funsten et al., 2013), along with measurements of more energetic ions (~50–500 keV) from the Radiation Belt Storm Probes Ion Composition Experiment (RBSPICE; Mitchell et al. (2013)). HOPE uses a top-hat electrostatic analyzer (ESA) in combination with time-of-flight (TOF) mass spectrometry to measure the major ionic constituents of the inner magnetosphere, H^+, He^+, and O^+. RBSPICE employs solid state detectors (SSDs) to record the total particle energy, in combination with a TOF system, to obtain measurements of the same ion species. We note that while HOPE measures ions down to the ~10 eV energy range, we focus our attention on the measurements at >1 keV because it is this hot population that contributes to the MS wave growth. While it is known that an intercalibration offset on the order of a factor of 2 may exist between the HOPE and RBSPICE ion intensities (Mouikis et al., 2019), we have not accounted for this small offset in our analysis below.

3. Observations

Figures 1a–1c presents an overview of the interplanetary and geomagnetic conditions for the ~40 h time interval that encompasses the MS wave event under investigation (event time highlighted with vertical blue lines). During the wave event, the magnetosphere was highly compressed, with a ~10-fold increase in solar wind dynamic pressure near the beginning of the event. Geomagnetic conditions were characterized by SYM-H > −30 nT with moderate AE activity (~300 nT) in the ~4 h leading up to and including the event. Panel (d) shows the electron number density and background magnetic field intensity from Van Allen Probe A during the MS wave event. The Probe was located inside of the plasmasphere during this time interval on

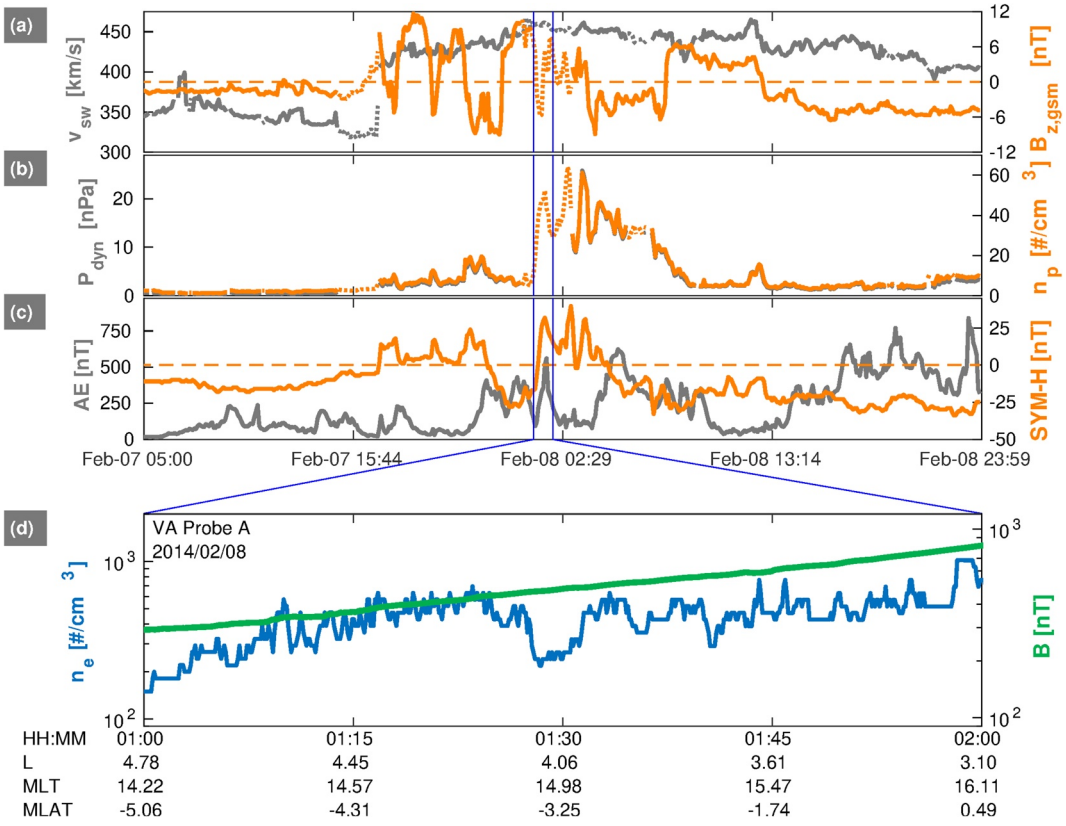

Figure 1. (a–c) Summary of the solar wind and geomagnetic conditions from the 5-min OMNI database. Gaps in the OMNI solar wind data are filled in using time-shifted WIND measurements (broken/dotted lines; see supporting information). The time interval of MS wave activity is indicated with vertical blue lines. (d) Van Allen Probe A observations of the electron number density and magnetic field strength during the MS wave event.

the inbound leg of its orbit in the afternoon magnetic local time (MLT) sector, as indicated by the magnetic ephemeris values shown below panel (d). These values were calculated from the Olson and Pfitzer (1977) "quiet" magnetic field model and the McIlwain L parameter is used throughout this study.

3.1. Wave Observations

Figure 2 presents an overview of the MAG data processed as described above during the MS wave event. In panels (a–d), we see a series of discrete MS waves excited with properties consistent with those described in Section 1. The waves are observed near the magnetic equator, are dominantly compressional with the strongest amplitudes in the field-aligned direction (B_z), and have large root-mean square (RMS) amplitudes reaching ~1 nT. Panel (e) shows the power spectral density in the B_z component at the time of maximum wave power, 01:38:20 UTC. In contrast with the MS waves typically reported in the literature, however, these waves are observed at harmonics of the local He^{++} gyrofrequency, $f_{cHe^{++}}$ (denoted f_c in the figure), with the oscillation frequencies closely tracking the time evolution of the gyrofrequency.

Figure 3a shows the same data that is plotted in Figure 2c, followed by the spin-plane electric field in panels (b) and (c). Here, we clearly see the first three MS wave harmonics in the electric field components, confirming their electromagnetic character. We note that the DC electric field measurement on Probe A was beginning to degrade at this time, visible as the sporadic noise below ~5 Hz. Calculations of the wave normal angle, ellipticity, and planarity are shown in panels (d–f), where the singular-value decomposition (SVD) method of Santolík et al. (2003) has been used. While the higher harmonics are nearly perpendicularly propagating with wave normal angles ~ 90°, note that the obliquity decreases in the lower harmonics. We will return to this point later. Similarly, the waves are nearly linearly polarized at the higher harmonics and

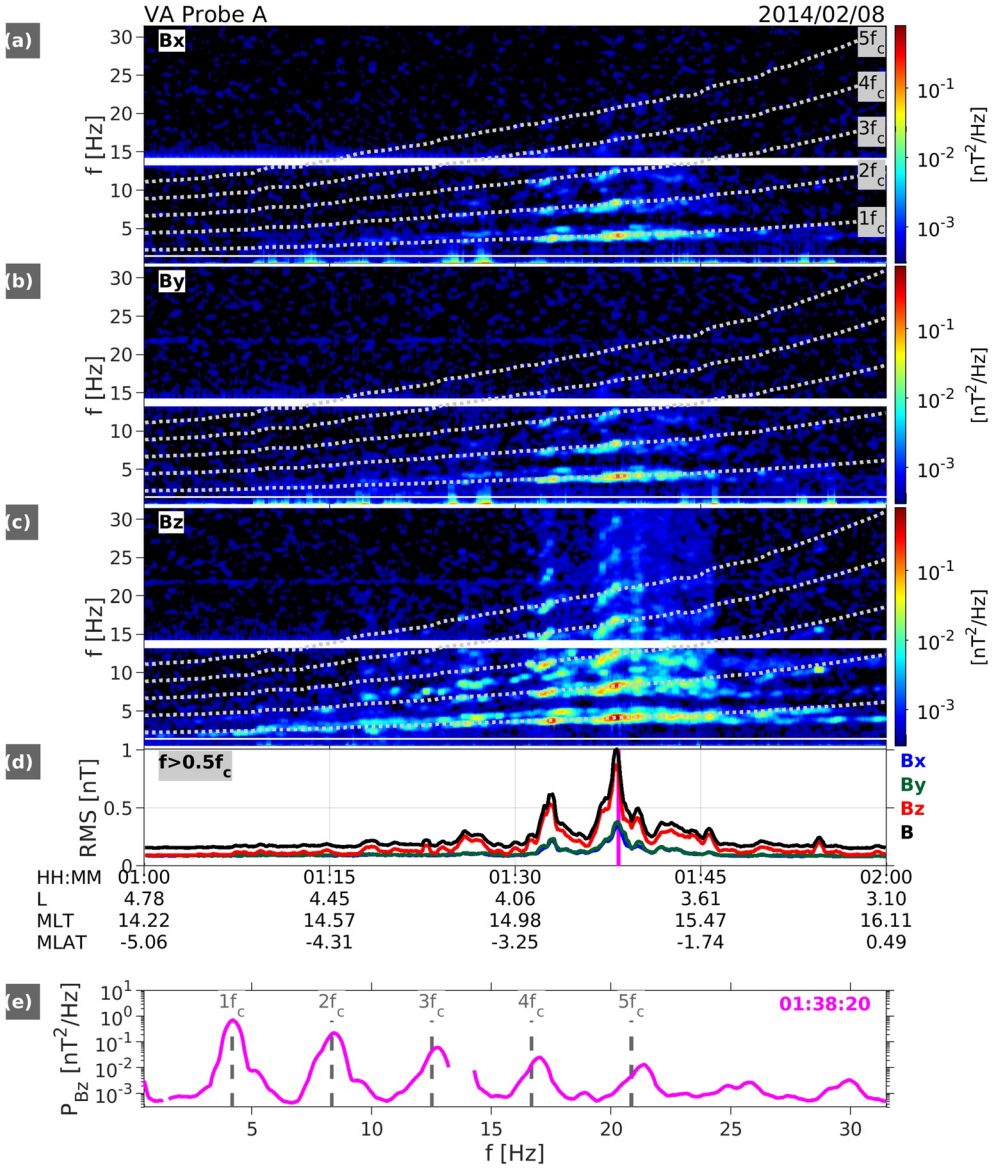

Figure 2. Summary of MS wave observations. (a–c) Dynamic spectrograms of wave power spectral density for the perpendicular (B_x, B_y) and field-aligned (B_z) magnetic field components. The power spectral densities are smoothed with a 15-point frequency window (~0.5 Hz). (d) RMS wave power. (e) B_z wave power spectral density at the time of wave power maximum (magenta vertical line in panel (d)). The observed harmonics are spaced at multiples of the local He^{++} gyrofrequency, $f_{cHe^{++}}$ (the label f_c denotes $f_{cHe^{++}}$); note that $f_{cHe^{++}} = \frac{1}{2} f_{cH+}$ and $f_{cHe^{++}} = 2\, f_{cHe^{+}}$, where f_{cH+} and $f_{cHe^{+}}$ represent the proton and singly ionized-helium gyrofrequencies, respectively. Various known noise lines have been filtered out from the spectra (spin tones and noise at 1.4 and 14 Hz).

become increasingly left-handed in the lower harmonics. The large wave planarities (on the order of unity) indicate that the single plane wave assumption required for the SVD analysis is valid.

3.2. Particle Observations

Figure 4a shows a summary of helium ion measurements from the HOPE and RBSPICE instruments for five consecutive orbits centered on the MS wave event time. This time interval is indicated with a magenta bar at the top of both panels (a) and (b). The flux measurements have been converted to phase space den-

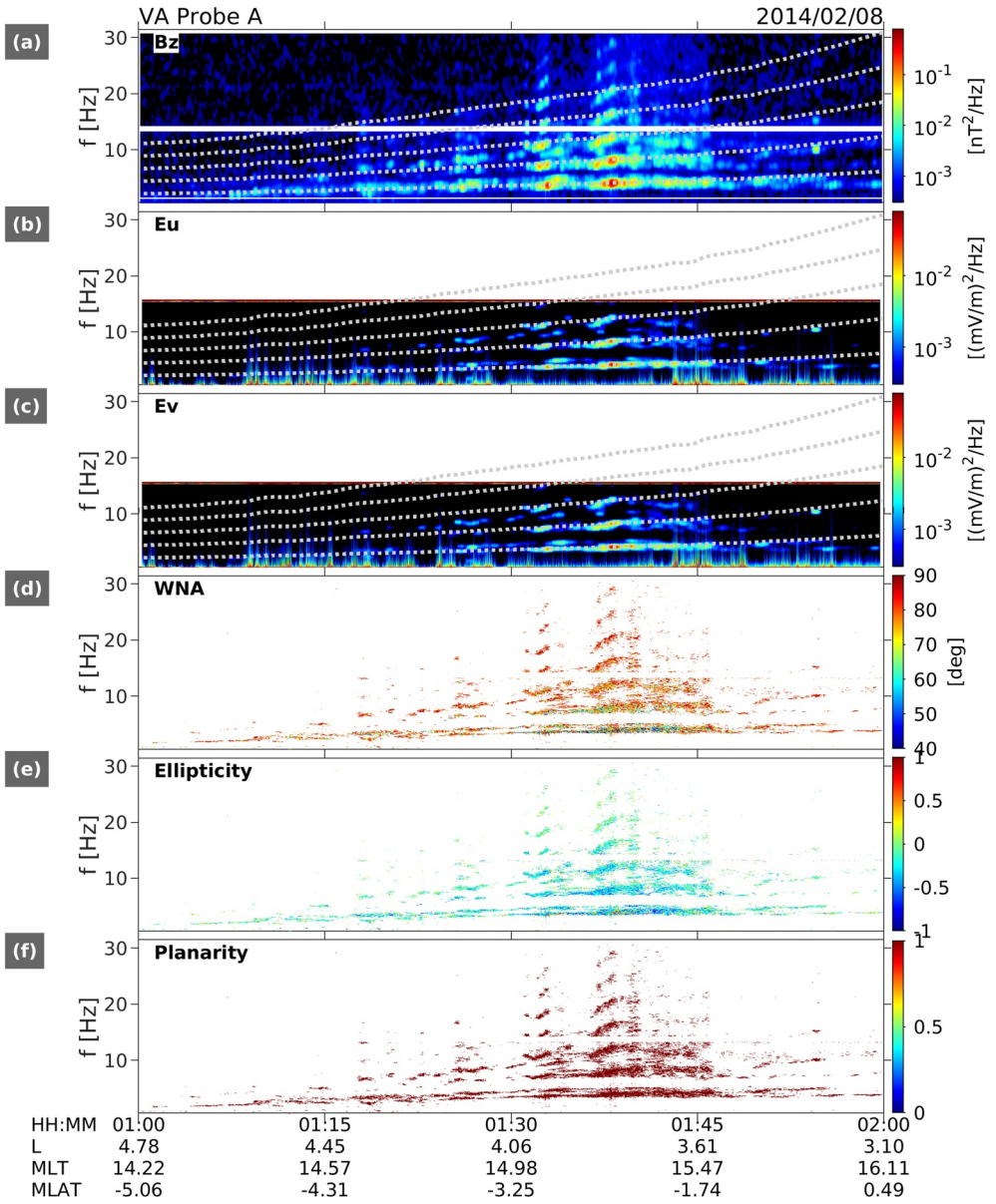

Figure 3. (a–c) Dynamic spectrograms of wave power spectral density for the field-aligned magnetic field (B_z) and spin-plane (E_u, E_v) electric field components. The power spectral densities are smoothed with a 15-point frequency window (~0.5 Hz). Note that the time resolution of the electric field measurements is a factor-of-two coarser than the magnetic field measurements, resulting in different Nyquist frequencies (16 vs. 32 Hz, respectively). (d–f) Wave normal angle, ellipticity (polarization), and planarity. These data are not smoothed and are only displayed for B_z wave power greater than $\sim 3\times10^{-3}$ nT^2/Hz. The gyroharmonic lines are not shown in these three panels.

sity (PSD) as a function of ion kinetic energy in the usual manner (e.g., Sheldon & Hamilton, 1993). In the HOPE energy range (<50 keV), the data are not displayed near perigee (vertical regions of white), while in the RBSPICE energy range (>60 keV), the data are not displayed at $L < 4$. We mask the HOPE data in this low-L region because the instrument changes modes near perigee to prevent damage to the foils used in the TOF subsystem from exposure to the intense O^+ flux near perigee (Funsten et al., 2013). In addition, there are uncertainties in the measurements near perigee due to potential inner belt proton contamination. The species-resolved RBSPICE ion data are not available below $L = 4$ during this event because the instrument's high-voltage system was typically disabled in this region to prevent premature aging and to maintain instrument health (Mitchell et al., 2013).

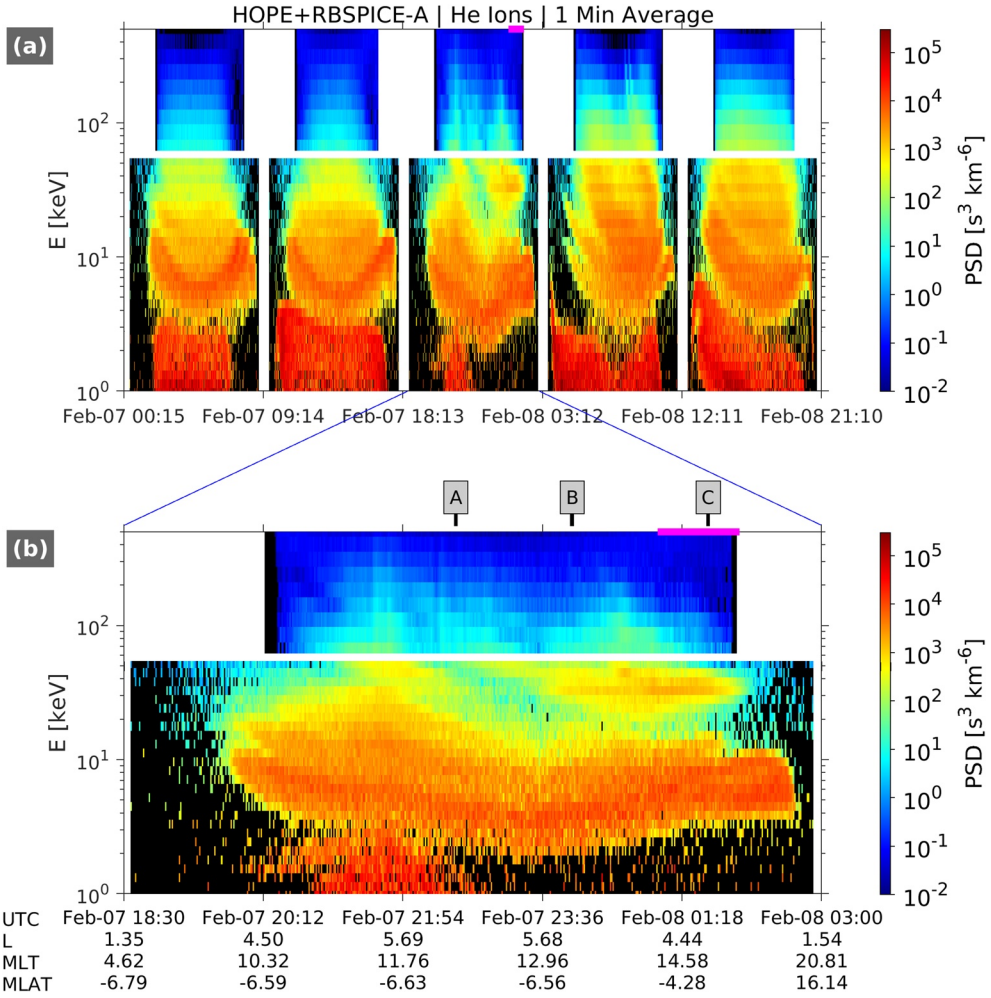

Figure 4. Summary of helium ion observations from Van Allen Probe A. (a) Five consecutive orbits of the measured helium ion phase space density are plotted versus energy and time. These data are averaged over all look directions and binned on a 1-min time cadence. Data gaps (white) are due to instrument modes changes at low L near perigee and the gap in instrument energy coverage near 50 keV. (b) A zoom in on the 3^{rd} orbit with the MS wave event interval indicated with a solid magenta line at the top of the panel. The A, B, and C labels indicate the times of the velocity space distributions shown in Figure 5.

In Figure 4a, note the multiple injections of higher energy helium ions (~100 keV) observed on the third orbit relative to the previous two "quiet" orbits. The injections are fairly dispersed in energy, indicating that the injection site is some distance from the spacecraft's orbital location (the spacecraft apogee is near 1300h MLT on this orbit). Note especially that on the inbound portion of the third orbit (see panel (b)), a spectral inversion develops near 30 keV in association with the injections, where the PSD is enhanced relative to the adjacent energies above and below 30 keV. This suggests that a helium ring distribution has formed at this time ($\partial f / \partial v_\perp > 0$), which will be analyzed in greater detail in the next section. Analogous plots for the other major ion species (H^+ and O^+) as well as the measurements from Van Allen Probe B are provided in the supporting information.

4. Discussion

The MS wave observations, in particular the discrete frequency spacing at integer harmonics of the local He^{++} gyrofrequency, suggest the presence of an unstable He^{++} distribution. However, we emphasize that neither HOPE nor RBSPICE explicitly provide He^{++} measurements. This lack of ion charge-state

identification is an unfortunate limitation of many space-borne particle sensors. We thus provide additional lines of reasoning so that we can make use of the available particle measurements in our analysis.

4.1. Helium Ring Distribution and Interpretation of the Ion Measurements

In the energy range of interest (~100 keV), He^{++} is the primary helium constituent at higher L (e.g., $L > 6.5$), while He^{+} dominates at lower L (Kremser et al., 1993; Cohen et al., 2017). These helium ions, presumably of solar wind origin, enter the magnetosphere via magnetotail reconnection and are convected and injected earthward as He^{++} ions (Mitchell et al., 2018). The He^{++} ions are adiabatically energized through their earthward motion and are subsequently lost through charge exchange on a timescale of a few hours (e.g., Daglis et al., 1999) and other processes (e.g., magnetopause loss). The charge exchange process between energetic He^{++} and the exospheric neutral geocorona (thermal hydrogen atoms) leaves behind an energetic He^{+} ion and a thermal energy H^{+} ion. Thus, as the energetic He^{+} ions produced by charge exchange constitute one of the primary sources of He^{+} in the inner magnetosphere (e.g., Kremser et al., 1993), we argue that the measurements of He^{+} injections serve as a proxy for He^{++} during the MS wave event. Specifically, since the helium ions are freshly injected, we can reasonably expect a significant fraction of those observed to be He^{++}, before they have had time to charge exchange into He^{+}. We now proceed under this assumption, with the expectation that the energy and angular distributions of the observed He^{+} ions are representative of the injected He^{++} population. In the supporting information, we present additional analysis to support this interpretation, exploiting the factor-of-two difference in the expected adiabatic energy gain between He^{+} and He^{++} during the observed injections. The analysis suggests that the injected helium ions observed by RBSPICE on the inbound leg of the orbit are in fact He^{++}. As described in the supporting information, the situation is more complicated for the HOPE measurements. Since HOPE measures mass per charge, He^{+} and He^{++} are in principle separated, though only He^{+} is computed from the TOF matrix and reported in the data products. However, we again argue that since HOPE observes a significant amount of He^{+} in this event, which could have resulted from He^{++} charge exchange, this indicates that there is likely also He^{++} present in the HOPE energy range.

Figure 5 shows snapshots of the helium-ion velocity-space distributions observed at the three times marked A, B, and C above panel (b) in Figure 4. In Figure 5a (before the helium ion injection), we see an approximately isotropic, monotonically decreasing profile of PSD, $f(v)$. In panel (b) (at the outset of the injection), we see the initial development of a positive gradient in PSD, $\partial f / \partial v_{\perp} > 0$, which has further developed in panel (c) during the MS wave event. This ring distribution is likely formed through an interplay between source (e.g., injection) and loss processes, in particular noting the highly compressed magnetosphere that likely results in enhanced ion loss to the dayside magnetopause during this time interval. In the next section, we show that this unstable distribution is sufficient to generate He^{++} MS waves. We note that particle velocity is independent of charge state for a given kinetic energy, so that the velocity values shown in Figure 5 are the same for He^{+} and He^{++}. And as mentioned above, a ring distribution is also observed in both the H^{+} and O^{+} measurements from Probe A (H^{+}/O^{+} velocity space distributions not shown here, but see the PSD summary plots in the supporting information).

4.2. Linear Growth Rate Analysis

To support the interpretation of the observed waves as He^{++} MS modes, we present a linear growth rate analysis using the in-situ plasma and field parameters. The wave dispersion relation and growth rates are calculated assuming an electromagnetic linear dispersion relation for bi-Maxwellian ring-beam velocity distributions (Umeda et al., 2012). Specifically, we consider a plasma that consists of electrons, protons, and He^{++}, each of which is assumed to follow a bi-Maxwellian ring-beam ("rb") velocity distribution:

$$f_{rb}\left(v_{\parallel}, v_{\perp}; n, a_{\parallel}, a_{\perp}, v_b, v_r\right) = \frac{n}{\pi^{1.5} a_{\parallel} a_{\perp}^2 C_r} \exp\left(-\frac{\left(v_{\parallel} - v_b\right)^2}{a_{\parallel}^2}\right) \exp\left(-\frac{\left(v_{\perp} - v_r\right)^2}{a_{\perp}^2}\right) \quad (1)$$

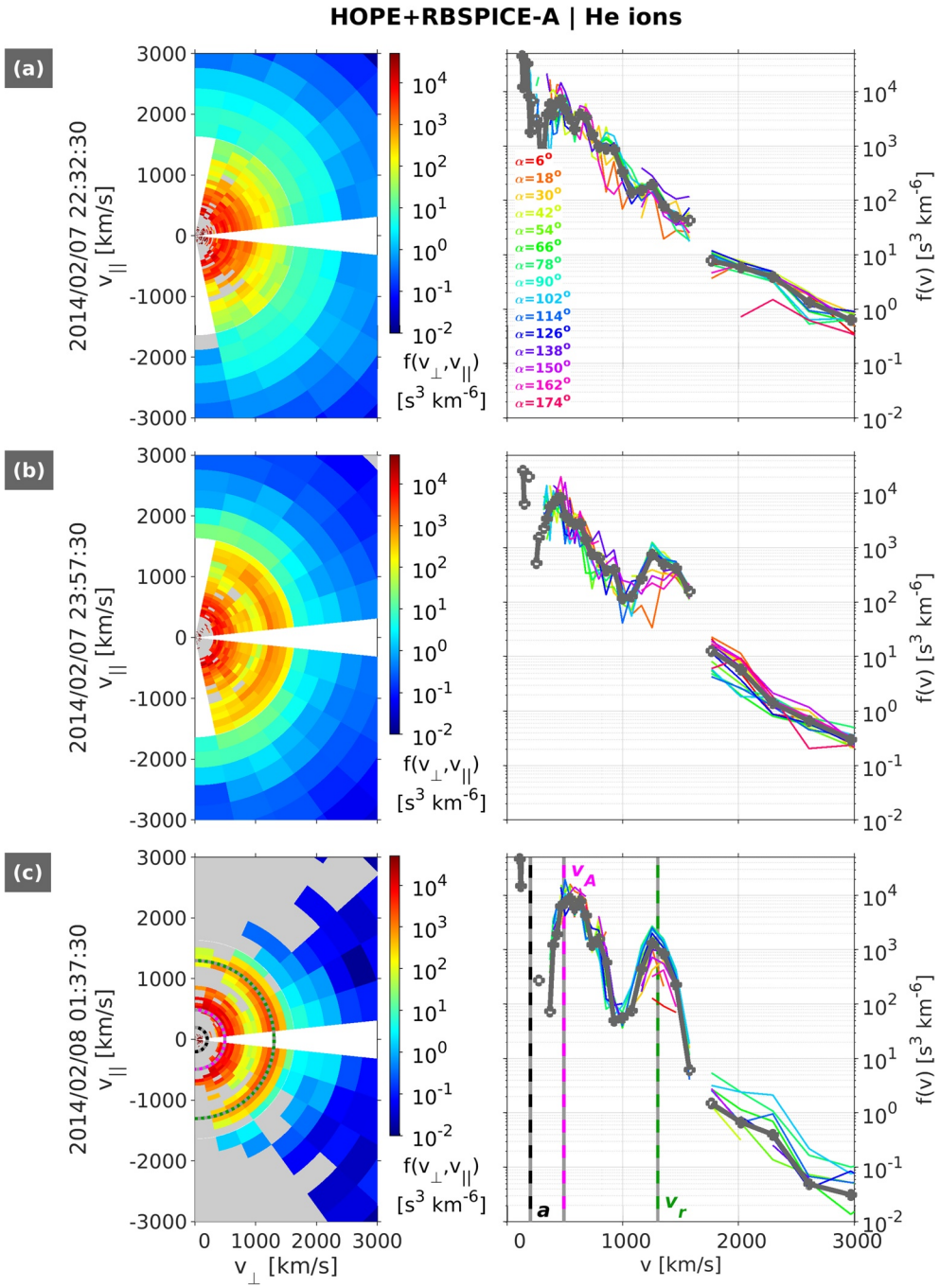

Figure 5. (a–c) Helium ion velocity space distributions for the three times indicated in Figure 4b. These data are averaged on a 5-min time cadence. The left column shows the distributions plotted in ($v_\perp$,$v_\parallel$)-space, while the right column shows the same data plotted versus velocity for different equatorial pitch angles (color). The dark gray line is the average over all pitch angles. In the left column, a gray color indicates a zero-flux value, while a white color indicates that this region of phase space is not observed (e.g., particles near the loss cone and/or magnetic equator). In panel (c), the ring velocity (v_r, dashed green), ring thermal velocity (a, dashed black), and Alfvén velocity (v_A, dashed magenta) are indicated.

Table 1
Parameters Used in Calculating the Wave Dispersion Relation and Growth Rate[a]

Species	Distribution type	n [#/cm^3]	$T_\parallel = T_\perp$[eV]	v_r[km/s]	v_b[km/s]
e^-	Maxwellian	500	10	0	0
H^+	Maxwellian	475	10	0	0
He^{++}	Maxwellian	22.5	500	0	0
He^{++}	Ring-beam	2.5	835	1,300	0

[a]$B_0 = 539$ nT is assumed in all calculations.

where:

$$C_r\left(a_\perp, v_r\right) = \exp\left(-\frac{v_r^2}{a_\perp^2}\right) + \sqrt{\pi}\,\frac{v_r}{a_\perp}\,\mathrm{erfc}\left(-\frac{v_r}{a_\perp}\right) \tag{2}$$

Here, n denotes the plasma number density, a denotes the thermal velocity, and the temperature is given by $T_s = \frac{1}{2} m_s a_s^2$ for species s. The directions parallel and perpendicular to the background magnetic field, B_0, are indicated by $\parallel$ and $\perp$, respectively. The ring and beam velocities are indicated by v_r and v_b, respectively, and erfc denotes the complementary error function. Note that this bi-Maxwellian ring-beam distribution reduces to the usual bi-Maxwellian distribution by setting $v_r = v_b = 0$.

The plasma and field parameters needed to evaluate Equation 1 and Equation 2 are obtained from the in-situ measurements as follows. The electron density, n_e, is derived from the upper hybrid resonance frequency measured by the HFR instrument on EMFISIS, while B_0 is obtained from the MAG sensor on EMFISIS. The values used in our calculations (see Figure 1d) were selected around the time labeled by "C" in Figure 4 and are shown in Table 1. The He^{++} ring thermal velocity, $a = 200$ km/s, and ring velocity, $v_r = 1300$ km/s, are inferred from the in-situ ion data at the corresponding time (Figure 5c). Here, we have assumed an ion composition of 95% H^+ and 5% He^{++}, and that the He^{++} ring accounts for 10% of the total He^{++} concentration. In the supporting information, we present an analysis of ULF wave magnetoseismology that supports our assumption that the plasmspheric cold ion population is dominated by H^+ around the time of the MS wave event.

We note that with a proton-dominated plasma, changing the ion composition (e.g., by including O^+) does not significantly change the dispersion relation and, thus, does not change the main results of our instability analysis below. For example, we have calculated the dispersion relation with an assumed ion composition of 90%/5%/5% ($H^+/He^{++}/O^+$) and compared with our assumption of 95%/5% (H^+/He^{++}). We find that the dispersion relation near the $f_{cHe^{++}}$ harmonics is essentially unchanged for the wave normal angles considered in our analysis below (not shown here). With regard to the assumption that the He^{++} ring accounts for 10% of the total He^{++} concentration, we note that the concentration of the He^{++} ring linearly controls the absolute values of the linear growth rate. However, it does not affect the frequency dependence and the relative relation of the linear growth rate of the different harmonic bands. For example, we have calculated the linear growth rate with a 6% He^{++} ring concentration and the results are very similar to our calculations shown below where a 10% assumption is used (not shown here).

We also assume that $T_\parallel = T_\perp = T$ (i.e., $a_\parallel^2 = a_\perp^2 = a^2$). The temperature of the Maxwellian He^{++} is assumed to be 500 eV to account for the warm He^{++} of (presumably) solar wind origin. Finally, we calculate that the ratio of the ring velocity to the Alfvén velocity is ~2.65, where we have computed a multi-ion Alfvén speed of $v_A = B_0 / \sqrt{\mu_0 m_i n_i} \approx 490$ km/s under the assumption of charge neutrality ($n_i = n_e = 500$ #/cm^3) and with an ion mass, $m_i = 0.95 m_H + 0.05 m_{He}$.

With these parameters in hand (summarized in Table 1), the wave dispersion relations and linear growth rates are calculated for two selected wave normal angles, $\theta = 40°$ and $\theta = 85°$, for the first 7 harmonics

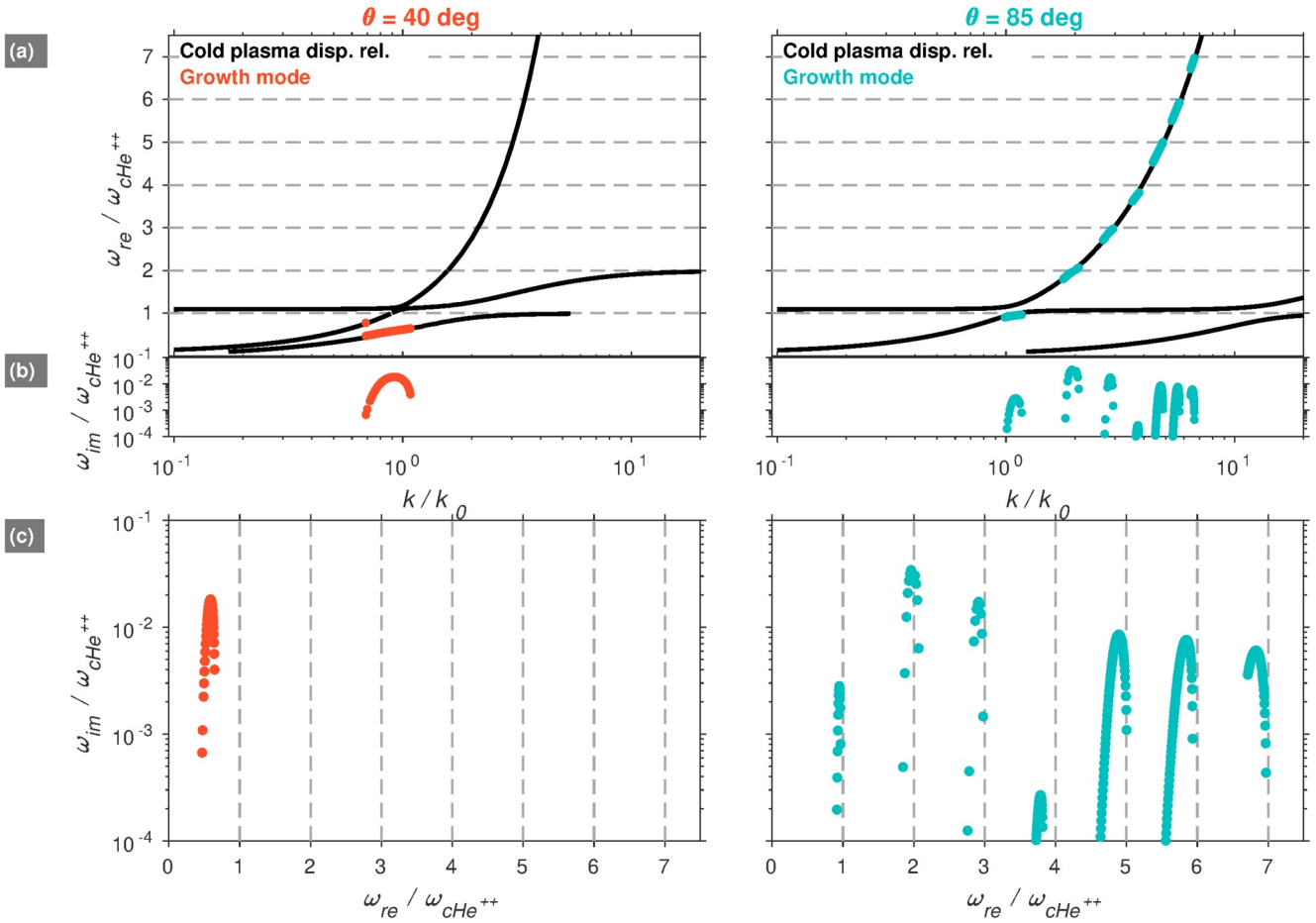

Figure 6. (a) Calculated dispersion relation for wave normal angles (θ) of 40° (left column, orange) and 85° (right column, turquoise). The cold plasma dispersion relation is shown in black and the horizontal dashed lines mark the harmonics of the He^{++} gyrofrequency ($\omega_{cHe^{++}}$). (b) Linear growth rate as a function of normalized wavenumber. Note that only positive growth rates are plotted. The wave frequencies (ω_{re}) and growth rates (ω_{im}) are normalized by $\omega_{cHe^{++}}$, while the wavenumber (k) is normalized by $k_0 = \omega_{cHe^{++}}/v_A$. (c) Linear growth rate as a function of wave frequency with the He^{++} gyrofrequency harmonics indicated with vertical dashed lines. Note the left column shows the He^{++} band EMIC wave mode, while the right column shows He^{++} and H^{+} band MS wave modes.

of the He^{++} gyrofrequency. Here, we have used an electromagnetic linear dispersion relation solver for Maxwellian ring-beam velocity distributions (following Umeda et al. (2012)) and the results are shown in Figure 6. In panel (a) at θ = 40°, the dispersion relation is such that the propagation is in the He^{++} EMIC mode with left-handed polarization, while in the θ = 85° panel the propagation is in the He^{++} MS mode with linear polarization. These calculations confirm the viability of our proposed interpretation - that the observed MS waves are generated by an He^{++} ring distribution. For example, in the quasi-perpendicular wave normal case (θ = 85°), the regions of maximum wave growth are closely aligned with the He^{++} gyrofrequency harmonics. These numerical results are consistent with the observed wave parameters shown in Figure 3. Specifically, in Figure 3d, we see that near the fundamental mode, the waves are propagating with moderate wave normal angles in the 40°- 60° range with a mixture of linear and left-handed polarizations, while at the higher harmonics (5^{th}-7^{th}), the waves are nearly perpendicularly propagating with linear polarization. We note that both the EMIC and ion Bernstein wave instabilities are driven by the He^{++} ring distribution, which is consistent with Min et al. (2016). Overall, the demonstrated agreement between theory and observation adds additional evidence that the free energy source for the observed MS waves is an unstable He^{++} ring distribution.

5. Summary and Conclusions

We present results from an event observed on Van Allen Probe A where MS waves were detected at integer multiples of the local He^{++} gyrofrequency. The event occurred under moderately disturbed geomagnetic conditions with the magnetosphere highly compressed, and with modest injection activity (AE ∼300 nT) leading up to and including the event interval. The available ion measurements from Probe A suggest the presence of helium ion injections that lead to a ring distribution in velocity space. Using the observed wave and plasma parameters, we calculate linear growth rates that demonstrate that the MS waves can be generated from an unstable He^{++} ring distribution. To our knowledge, all studies of magnetospheric MS waves in the published literature report the wave harmonics at integer multiples of the local proton gyrofrequency and explain their generation via a proton ring distribution. In contrast, the work presented here represents the first report of MS waves associated with, and generated from, He^{++} ions.

While He^{++} ions are not believed to play a significant role inner magnetospheric dynamics due to their rapid loss via charge exchange and other processes, we have demonstrated that freshly injected He^{++} ions can produce intense MS waves (∼0.5–1 nT) that may in turn influence other populations (e.g., radiation belt electron acceleration and ring current ion scattering, as noted in Section 1). Given that helium ion injections are typically dominated by He^{++} (Mitchell et al., 2018), their role in inner magnetospheric dynamics may be more influential than previously believed.

We emphasize our use of DC electric and magnetic field measurements, as a significant fraction of prior studies of MS waves, including a number of statistical surveys, used search-coil magnetometers and/or waveform receivers. These sensors may not be able to resolve the low-frequency harmonic structure in the 1–30 Hz range, which can be present without the simultaneous occurrence of higher harmonics (Posch et al., 2015).

We argue that the observations and numerical calculations presented suggest that the most plausible explanation for the observed frequency spacing in the MS waves is their local generation via an He^{++} ring distribution. However, there are other possible mechanisms that could explain the observed harmonic structure. For example, mechanisms that can produce half-integer or even-integer harmonics, such as nonlinear wave-wave interactions, could also produce the observed structure. However, we note that for the other major ionic constituents of the inner magnetosphere (H^+, He^+, and O^+) to produce the observed harmonic spacing, this would require a mechanism that produces half-integer, factor-of-2, and factor-of-8 multiples of the corresponding gyrofrequencies, respectively. Nonlinear interactions can produce fractional integer resonances (e.g., Fu et al. (2015) for whistler waves), though this will lead to a variable frequency spacing at 1/2, 1/3, … multiples in the harmonics. We emphasize that the observed equal spacing in the harmonics favors the interpretation of integer resonances. We also note that such integer frequency spacing could be produced by another ion species (e.g., H^+, He^+, or O^+) if the observed MS waves were generated nonlocally. However, we find this to be an unlikely scenario as well, since the waves would have to propagate radially at least 1 L-shell (or more, depending on the species) from the local source region to the spacecraft, assuming $B_0 \sim L^{-3}$. Overall, given the increased complexity of such mechanisms and the lack of additional supporting evidence, we favor the interpretation of a local MS wave excitation via an unstable He^{++} ring distribution.

Finally, we note that any ion with mass-to-charge ratio of $M / Q = 2$ could also produce MS waves with the observed harmonic spacing, assuming the ions exist in sufficient quantities at the necessary energies for such an excitation. It is generally believed that there are two possible species of $M / Q = 2$ ions in the inner magnetosphere: deuterons and He^{++} (e.g., Matsuda et al., 2015). Deuterons likely originate from the ionosphere and are most typically found at low altitudes and at thermal energies, while He^{++} likely originates from the solar wind and is found predominantly at higher L and at ring current energies. We note that recent work has used plasma wave observations to infer the presence of cold $M / Q = 2$ ions, likely deuterons, at low L ($L < 3$; Matsuda et al. (2015); Matsuda et al. (2016); Miyoshi et al. (2019)). As there is no known process to energize deuterons (or other $M / Q = 2$ ions) to the ∼100 keV energy range studied here, nor a mechanism that can explain their injection to $L \approx 4$ from the outer magnetosphere, it seems most plausible that the ions under investigation here are indeed He^{++}.

Data Availability Statement

All of the data used in this manuscript are in the public domain and accessible from the Van Allen Probes Science Gateway at https://rbspgway.jhuapl.edu/. We thank the Van Allen Probe instrument teams for their tireless efforts to produce a high-quality data set. We acknowledge use of NASA/GSFC's Space Physics Data Facility's CDAWeb service and OMNI data.

Acknowledgments
Two authors (S. G. Claudepierre and L. Chen) are grateful for funding provided by the National Science Foundation's Geospace Environment Modeling program (award numbers AGS-1702960 and AGS-1854440). L. Chen was also supported by the NASA Heliophysics Supporting Research program (award number NNX17AI52 G). K. Takahashi was supported by the NASA Heliophysics Guest Investigators Open program (award number 80NSSC21K0453). The RBSPICE instrument was supported by JHU/APL subcontract 937836 to the New Jersey Institute of Technology under NASA Prime contract NAS5-01072. The EMFISIS instrument was supported by JHU/APL subcontract 921647 under NASA Prime contract NAS5-01072. The EFW instrument was supported by JHU/APL subcontract 922613 (RBSP-EFW) under NASA Prime contract NAS5-01072. Processing and analysis of the HOPE data was supported by Energetic Particle, Composition, and Thermal Plasma (RBSP-ECT) investigation funded under NASA Prime contract NAS5-01072. We thank Drew Turner for preparing the ARTEMIS solar wind data shown in the supporting information and Lynn Kistler and Brian Larsen for helpful discussions on the interpretation of the HOPE measurements.

References

Balikhin, M. A., Shprits, Y. Y., Walker, S. N., Chen, L., Cornilleau-Wehrlin, N., Dandouras, I., et al. (2015). Observations of discrete harmonics emerging from equatorial noise. *Nature Communications*, *6*, 7703. https://doi.org/10.1038/ncomms8703

Boardsen, S. A., Gallagher, D. L., Gurnett, D. A., Peterson, W. K., & Green, J. L. (1992). Funnel-shaped, low-frequency equatorial waves. *Journal of Geophysical Research*, *97*(A10), 14967–14976. https://doi.org/10.1029/92JA00827

Boardsen, S. A., Hospodarsky, G. B., Kletzing, C. A., Pfaff, R. F., Kurth, W. S., Wygant, J. R., & MacDonald, E. A. (2014). Van Allen Probe observations of periodic rising frequencies of the fast magnetosonic mode. *Geophysical Research Letters*, *41*(23), 8161–8168. https://doi.org/10.1002/2014GL062020

Chen, L. (2015). Wave normal angle and frequency characteristics of magnetosonic wave linear instability. *Geophysical Research Letters*, *42*(12), 4709–4715. https://doi.org/10.1002/2015GL064237

Chen, L., & Thorne, R. M. (2012). Perpendicular propagation of magnetosonic waves. *Geophysical Research Letters*, *39*(14), L14102. https://doi.org/10.1029/2012GL052485

Chen, L., Thorne, R. M., Jordanova, V. K., & Horne, R. B. (2010). Global simulation of magnetosonic wave instability in the storm time magnetosphere. *Journal of Geophysical Research*, *115*(A11), A11222. https://doi.org/10.1029/2010JA015707

Chen, L., Thorne, R. M., Jordanova, V. K., Thomsen, M. F., & Horne, R. B. (2011). Magnetosonic wave instability analysis for proton ring distributions observed by the LANL magnetospheric plasma analyzer. *Journal of Geophysical Research*, *116*(A3), A03223. https://doi.org/10.1029/2010JA016068

Cohen, I. J., Mitchell, D. G., Kistler, L. M., Mauk, B. H., Anderson, B. J., Westlake, J. H., et al. (2017). Dominance of high-energy (>150 keV) heavy ion intensities in Earth's middle to outer magnetosphere. *Journal of Geophysical Research*, *122*(9), 9282–9293. https://doi.org/10.1002/2017JA024351

Curtis, S. A., & Wu, C. S. (1979). Gyroharmonic emissions induced by energetic ions in the equatorial plasmasphere. *Journal of Geophysical Research*, *84*(A6), 2597–2607. https://doi.org/10.1029/JA084iA06p02597

Daglis, I. A., Thorne, R. M., Baumjohann, W., & Orsini, S. (1999). The terrestrial ring current: Origin, formation, and decay. *Reviews of Geophysics*, *37*, 407–438. https://doi.org/10.1029/1999RG900009

Fu, H. S., Cao, J. B., Zhima, Z., Khotyaintsev, Y. V., Angelopoulos, V., Santolík, O., et al. (2014). First observation of rising-tone magnetosonic waves. *Geophysical Research Letters*, *41*(21), 7419–7426. https://doi.org/10.1002/2014GL061867

Fu, X., Guo, Z., Dong, C., & Gary, S. P. (2015). Nonlinear subcyclotron resonance as a formationmechanism for gaps in banded chorus. *Geophysical Research Letters*, *42*(9), 3150–3159. https://doi.org/10.1002/2015GL064182

Funsten, H. O., Skoug, R. M., Guthrie, A. A., MacDonald, E. A., Baldonado, J. R., Harper, R. W., et al. (2013). Helium, oxygen, proton, and electron (HOPE) mass spectrometer for the radiation belt storm probes mission. *Space Science Reviews*, *179*, 423–484. https://doi.org/10.1007/s11214-013-9968-7

Gary, S. P., Liu, K., Winske, D., & Denton, R. E. (2010). Ion Bernstein instability in the terrestrial magnetosphere: Linear dispersion theory. *Journal of Geophysical Research*, *115*(A12), A12209–n. https://doi.org/10.1029/2010JA015965

Gurnett, D. A. (1976). Plasma wave interactions with energetic ions near the magnetic equator. *Journal of Geophysical Research*, *81*(16), 2765–2770. https://doi.org/10.1029/JA081i016p02765

Hartley, D. P., Kletzing, C. A., Santolík, O., Chen, L., & Horne, R. B. (2018). Statistical properties of plasmaspheric hiss from Van Allen probes observations. *Journal of Geophysical Research*, *123*(4), 2605–2619. https://doi.org/10.1002/2017JA024593

Horne, R. B., & Thorne, R. M. (1998). Potential waves for relativistic electron scattering and stochastic acceleration during magnetic storms. *Geophysical Research Letters*, *25*, 3011–3014. https://doi.org/10.1029/98GL01002

Horne, R. B., Thorne, R. M., Glauert, S. A., Meredith, N. P., Pokhotelov, D., & Santolík, O. (2007). Electron acceleration in the van allen radiation belts by fast magnetosonic waves. *Geophysical Research Letters*, *34*, L17107. https://doi.org/10.1029/2007GL030267

Horne, R. B., Wheeler, G. V., & Alleyne, H. S. C. K. (2000). Proton and electron heating by radially propagating fast magnetosonic waves. *Journal of Geophysical Research*, *105*(A12), 27597–27610. https://doi.org/10.1029/2000JA000018

Hrbáčková, Z., Santolík, O., Němec, F., Macúšová, E., & Cornilleau-Wehrlin, N. (2015). Systematic analysis of occurrence of equatorial noise emissions using 10 years of data from the Cluster mission. *Journal of Geophysical Research*, *120*(2), 1007–1021. https://doi.org/10.1002/2014JA020268

Jordanova, V. K., Welling, D. T., Zaharia, S. G., Chen, L., & Thorne, R. M. (2012). Modeling ring current ion and electron dynamics and plasma instabilities during a high-speed stream driven storm. *Journal of Geophysical Research*, *117*, A00L08. https://doi.org/10.1029/2011JA017433

Kasahara, Y., Kenmochi, H., & Kimura, I. (1994). Propagation characteristics of the ELF emissions observed by the satellite Akebono in the magnetic equatorial region. *Radio Science*, *29*(4), 751–767. https://doi.org/10.1029/94RS00445

Kletzing, C. A., Kurth, W. S., Acuna, M., MacDowall, R. J., Torbert, R. B., Averkamp, T., et al. (2013). The Electric and Magnetic Field Instrument Suite and Integrated Science (EMFISIS) on RBSP. *Space Science Reviews*, *179*, 127–181. https://doi.org/10.1007/s11214-013-9993-6

Kremser, G., Wilken, B., Gloeckler, G., Hamilton, D. C., Ipavich, F. M., Kistler, L. M., & Tanskanen, P. (1993). Origin, transport, and losses of energetic He(+) and He(2+) ions in the magnetosphere of the Earth - AMPTE/CCE observations. *Annales de Geophysique*, *11*(5), 354–365.

Kurth, W. S., De Pascuale, S., Faden, J. B., Kletzing, C. A., Hospodarsky, G. B., Thaller, S., & Wygant, J. R. (2015). Electron densities inferred from plasma wave spectra obtained by the Waves instrument on Van Allen Probes. *Journal of Geophysical Research*, *120*(2), 904–914. https://doi.org/10.1002/2014JA020857

Li, J., Bortnik, J., Thorne, R. M., Li, W., Ma, Q., Baker, D. N., et al. (2016). Ultrarelativistic electron butterfly distributions created by parallel acceleration due to magnetosonic waves. *Journal of Geophysical Research*, *121*(4), 3212–3222. https://doi.org/10.1002/2016JA022370

Liu, K., Gary, S. P., & Winske, D. (2011). Excitation of magnetosonic waves in the terrestrial magnetosphere: Particle-in-cell simulations. *Journal of Geophysical Research*, *116*(A7), A07212. https://doi.org/10.1029/2010JA016372

Liu, K., Min, K., Feng, B., & Wang, Y. (2020). Excitation of oxygen ion cyclotron harmonic waves in the inner magnetosphere: Hybrid simulations. *Geophysical Research Letters*, *47*(20), e2020GL090575. https://doi.org/10.1029/2020GL090575

Liu, X., Chen, L., Yang, L., Xia, Z., & Malaspina, D. M. (2018). One-dimensional full wave simulation of equatorial magnetosonic wave propagation in an inhomogeneous magnetosphere. *Journal of Geophysical Research*, *123*(1), 587–599. https://doi.org/10.1002/2017JA024336

Ma, Q., Li, W., Chen, L., Thorne, R. M., Kletzing, C. A., Kurth, W. S., et al. (2014). The trapping of equatorial magnetosonic waves in the Earth's outer plasmasphere. *Geophysical Research Letters*, *41*(18), 6307–6313. https://doi.org/10.1002/2014GL061414

Ma, Q., Li, W., Thorne, R. M., & Angelopoulos, V. (2013). Global distribution of equatorial magnetosonic waves observed by THEMIS. *Geophysical Research Letters*, *40*(10), 1895–1901. https://doi.org/10.1002/grl.50434

Ma, Q., Li, W., Thorne, R. M., Bortnik, J., Kletzing, C. A., Kurth, W. S., & Hospodarsky, G. B. (2016). Electron scattering by magnetosonic waves in the inner magnetosphere. *Journal of Geophysical Research*, *121*(1), 274–285. https://doi.org/10.1002/2015JA021992

Maldonado, A. A., Chen, L., Claudepierre, S. G., Bortnik, J., Thorne, R. M., & Spence, H. (2016). Electron butterfly distribution modulation by magnetosonic waves. *Geophysical Research Letters*, *43*(7), 3051–3059. https://doi.org/10.1002/2016GL068161

Matsuda, S., Kasahara, Y., & Goto, Y. (2015). M/q = 2 ion distribution in the inner magnetosphere estimated from ion cyclotron whistler waves observed by the akebono satellite. *Journal of Geophysical Research*, *120*(4), 2783–2795. https://doi.org/10.1002/2014JA020972

Matsuda, S., Kasahara, Y., & Kletzing, C. A. (2016). Variation in crossover frequency of emic waves in plasmasphere estimated from ion cyclotron whistler waves observed by van allen probe a. *Geophysical Research Letters*, *43*(1), 28–34. https://doi.org/10.1002/2015GL066893

Mauk, B. H., Fox, N. J., Kanekal, S. G., Kessel, R. L., Sibeck, D. G., & Ukhorskiy, A. (2013). Science Objectives and Rationale for the Radiation Belt Storm Probes Mission. *Space Science Reviews*, *179*, 3–27. https://doi.org/10.1007/s11214-012-9908-y

Meredith, N. P., Horne, R. B., & Anderson, R. R. (2008). Survey of magnetosonic waves and proton ring distributions in the Earth's inner magnetosphere. *Journal of Geophysical Research*, *113*, 6213. https://doi.org/10.1029/2007JA012975

Min, K., Denton, R. E., Liu, K., Gary, S. P., & Spence, H. E. (2017). Ion bernstein instability as a possible source for oxygen ion cyclotron harmonic waves. *Journal of Geophysical Research*, *122*(5), 5449–5465. https://doi.org/10.1002/2017JA023979

Min, K., Liu, K., Denton, R. E., Němec, F., Boardsen, S. A., & Miyoshi, Y. (2020). Two-dimensional hybrid particle-in-cell simulations of magnetosonic waves in the dipole magnetic field: On a constant l-shell. *Journal of Geophysical Research*, *125*(10), e2020JA028414. https://doi.org/10.1029/2020JA028414

Min, K., Liu, K., & Gary, S. P. (2016). Scalings of alfvén-cyclotron and ion bernstein instabilities on temperature anisotropy of a ring-like velocity distribution in the inner magnetosphere. *Journal of Geophysical Research*, *121*(3), 2185–2193. https://doi.org/10.1002/2015JA022134

Mitchell, D. G., Gkioulidou, M., & Ukhorskiy, A. Y. (2018). Energetic ion injections inside geosynchronous orbit: Convection-and drift-dominated, charge-dependent adiabatic energization (W = qEd). *Journal of Geophysical Research*, *123*(8), 6360–6382. https://doi.org/10.1029/2018JA025556

Mitchell, D. G., Lanzerotti, L. J., Kim, C. K., Stokes, M., Ho, G., Cooper, S., et al. (2013). Radiation belt storm probes ion composition experiment (RBSPICE). *Space Science Reviews*, *179*(1–4), 263–308. https://doi.org/10.1007/s11214-013-9965-x

Miyoshi, Y., Matsuda, S., Kurita, S., Nomura, K., Keika, K., Shoji, M., et al. (2019). EMIC waves converted from equatorial noise due to m/q=2 ions in the plasmasphere: Observations from van allen probes and arase. *Geophysical Research Letters*, *46*(11), 5662–5669. https://doi.org/10.1029/2019GL083024

Mouikis, C. G., Bingham, S. T., Kistler, L. M., Farrugia, C. J., Spence, H. E., Reeves, G. D., et al. (2019). The storm-time ring current response to icmes and cirs using van allen probe observations. *Journal of Geophysical Research*, *124*(11), 9017–9039. https://doi.org/10.1029/2019JA026695

Mourenas, D., Artemyev, A. V., Agapitov, O. V., & Krasnoselskikh, V. (2013). Analytical estimates of electron quasi-linear diffusion by fast magnetosonic waves. *Journal of Geophysical Research*, *118*(6), 3096–3112. https://doi.org/10.1002/jgra.50349

Němec, F., Santolík, O., Gereová, K., Macúšová, E., de Conchy, Y., & Cornilleau-Wehrlin, N. (2005). Initial results of a survey of equatorial noise emissions observed by the Cluster spacecraft. *Planetary and Space Science*, *53*(1–3), 291–298. https://doi.org/10.1016/j.pss.2004.09.055

Němec, F., Santolík, O., Hrbáčková, Z., Pickett, J. S., & Cornilleau-Wehrlin, N. (2015). Equatorial noise emissions with quasiperiodic modulation of wave intensity. *Journal of Geophysical Research*, *120*(4), 2649–2661. https://doi.org/10.1002/2014JA020816

Němec, F., Santolík, O., Pickett, J. S., Hrbáčková, Z., & Cornilleau-Wehrlin, N. (2013). Azimuthal directions of equatorial noise propagation determined using 10 years of data from the Cluster spacecraft. *Journal of Geophysical Research*, *118*(11), 7160–7169. https://doi.org/10.1002/2013JA019373

Olsen, R. C., Shawhan, S. D., Gallagher, D. L., Green, J. L., Chappell, C. P., & Anderson, R. R. (1987). Plasma observations at the earth's magnetic equator. *Journal of Geophysical Research*, *92*(A3), 2385–2407. https://doi.org/10.1029/JA092iA03p02385

Olson, W. P., & Pfitzer, K. A. (1977). *Magnetospheric magnetic field modeling (Tech. Rep. No. Annual Report)*. McDonnell-Douglas Astronautics Co.

Ouyang, Z., Yuan, Z., Yu, X., & Yao, F. (2021). Narrowband magnetosonic waves near the lower hybrid resonance frequency in the inner magnetosphere: Wave properties and excitation conditions. *Journal of Geophysical Research*, *126*(1), 2020JA028158. https://doi.org/10.1029/2020JA028158

Perraut, S., Roux, A., Robert, P., Gendrin, R., Sauvaud, J.-A., Bosqued, J.-M., et al. (1982). A systematic study of ULF Waves Above FH+ from GEOS 1 and 2 Measurements and Their Relationships with proton ring distributions. *Journal of Geophysical Research*, *87*(A8), 6219–6236. https://doi.org/10.1029/JA087iA08p06219

Posch, J. L., Engebretson, M. J., Olson, C. N., Thaller, S. A., Breneman, A. W., Wygant, J. R., et al. (2015). Low-harmonic magnetosonic waves observed by the Van Allen Probes. *Journal of Geophysical Research*, *120*(8), 6230–6257. https://doi.org/10.1002/2015JA021179

Russell, C. T., Holzer, R. E., & Smith, E. J. (1969). Ogo 3 observations of elf noise in the magnetosphere: 1. spatial extent and frequency of occurrence. *Journal of Geophysical Research*, *74*(3), 755–777. https://doi.org/10.1029/JA074i003p00755

Russell, C. T., Holzer, R. E., & Smith, E. J. (1970). Ogo 3 observations of elf noise in the magnetosphere: 2. the nature of the equatorial noise. *Journal of Geophysical Research*, *75*(4), 755–768. https://doi.org/10.1029/JA075i004p00755

Santolík, O., Nemec, F., Gereová, K., Macúšová, E., Conchy, Y., & Cornilleau-Wehrlin, N. (2004). Systematic analysis of equatorial noise below the lower hybrid frequency. *Annales de Geophysique*, *22*(7), 2587–2595. https://doi.org/10.5194/angeo-22-2587-2004

Santolík, O., Parrot, M., & Lefeuvre, F. (2003). Singular value decomposition methods for wave propagation analysis. *Radio Science*, *38*(1), 1010. https://doi.org/10.1029/2000RS002523

Santolík, O., Parrot, M., & Němec, F. (2016). Propagation of equatorial noise to low altitudes: Decoupling from the magnetosonic mode. *Geophysical Research Letters*, *43*(13), 6694–6704. https://doi.org/10.1002/2016GL069582

Sheldon, R. B., & Hamilton, D. C. (1993). Ion transport and loss in the earth's quiet ring current. I-Data and standard model. *Journal of Geophysical Research*, *98*, 13. https://doi.org/10.1029/92JA02869

Thomsen, M. F., Denton, M. H., Jordanova, V. K., Chen, L., & Thorne, R. M. (2011). Free energy to drive equatorial magnetosonic wave instability at geosynchronous orbit. *Journal of Geophysical Research*, *116*(A8), A08220. https://doi.org/10.1029/2011JA016644

Tsurutani, B. T., Falkowski, B. J., Pickett, J. S., Verkhoglyadova, O. P., Santolik, O., & Lakhina, G. S. (2014). Extremely intense ELF magnetosonic waves: A survey of polar observations. *Journal of Geophysical Research*, *119*(2), 964–977. https://doi.org/10.1002/2013JA019284

Umeda, T., Matsukiyo, S., Amano, T., & Miyoshi, Y. (2012). A numerical electromagnetic linear dispersion relation for Maxwellian ring-beam velocity distributions. *Physics of Plasmas*, *19*(7), 072107. https://doi.org/10.1063/1.4736848

Usanova, M. E., Malaspina, D. M., Jaynes, A. N., Bruder, R. J., Mann, I. R., Wygant, J. R., & Ergun, R. E. (2016). Van Allen probes observations of oxygen cyclotron harmonic waves in the inner magnetosphere. *Geophysical Research Letters*, *43*(17), 8827–8834. https://doi.org/10.1002/2016GL070233

Wygant, J. R., Bonnell, J. W., Goetz, K., Ergun, R. E., Mozer, F. S., Bale, S. D., et al. (2013). The Electric Field and Waves Instruments on the Radiation Belt Storm Probes Mission. *Space Science Reviews*, *179*(1–4), 183–220. https://doi.org/10.1007/s11214-013-0013-7

Xiao, F., Zhou, Q., He, Z., & Tang, L. (2012). Three-dimensional ray tracing of fast magnetosonic waves. *Journal of Geophysical Research*, *117*(A6), A06208. https://doi.org/10.1029/2012JA017589

Xiao, F., Zhou, Q., He, Z., Yang, C., He, Y., & Tang, L. (2013). Magnetosonic wave instability by proton ring distributions: Simultaneous data and modeling. *Journal of Geophysical Research*, *118*(7), 4053–4058. https://doi.org/10.1002/jgra.50401

Xiao, F., Zong, Q., Wang, Y., He, Z., Su, Z., Yang, C., & Zhou, Q. (2014). Generation of proton aurora by magnetosonic waves. *Scientific Reports*, *4*, 5190. https://doi.org/10.1038/srep05190

Yang, C., Su, Z., Xiao, F., Zheng, H., Wang, Y., Wang, S., et al. (2017). A positive correlation between energetic electron butterfly distributions and magnetosonic waves in the radiation belt slot region. *Geophysical Research Letters*, *44*(9), 3980–3990. https://doi.org/10.1002/2017GL073116

Yuan, Z., Ouyang, Z., Yu, X., Huang, S., Yao, F., & Funsten, H. O. (2018). Global distribution of proton rings and associated magnetosonic wave instability in the inner magnetosphere. *Geophysical Research Letters*, *45*(19), 10160–10166. https://doi.org/10.1029/2018GL079999

Zhou, Q., Jiang, Z., Yang, C., He, Y., Liu, S., & Xiao, F. (2021). Correlated observation on global distributions of magnetosonic waves and proton rings in the radiation belts. *Journal of Geophysical Research*, *126*(1), e2020JA028354. https://doi.org/10.1029/2020JA028354

Zhou, R., Fu, S., Ni, B., Hua, M., Yi, J., Gu, X., et al. (2020). Parametric dependence of the formation of electron butterfly pitch angle distribution driven by magnetosonic waves. *Journal of Geophysical Research*, *125*(10), e2020JA027967. https://doi.org/10.1029/2020JA027967

References From the Supporting Information

Takahashi, K., & Denton, R. E. (2021). Nodal structure of toroidal standing alfvén waves and its implication for field line mass density distribution. *Journal of Geophysical Research*, *126*(5), e2020JA028981. https://doi.org/10.1029/2020JA028981

Takahashi, K., Denton, R. E., Kurth, W., Kletzing, C., Wygant, J., Bonnell, J., & MacDowall, R. (2015). Externally driven plasmaspheric ULF waves observed by the Van Allen Probes. *Journal of Geophysical Research*, *120*(1), 526–552. https://doi.org/10.1002/2014JA020373

Vira, A. D., Larsen, B. A., Skoug, R. M., & Fernandes, P. A. (2021). Bayesian model for hope mass spectrometers on van allen probes. *Journal of Geophysical Research*, *126*(3), e2020JA028862. https://doi.org/10.1029/2020JA028862